Multiband Microwave Passive Devices Using Generalized Negative-Refractive-Index Transmission Lines (Invited Paper)

Colan G. M. Ryan, George V. Eleftheriades

Department of Electrical and Computer Engineering, University of Toronto, Toronto, Canada.

Received 31 January 2012; accepted 3 February 2012

ABSTRACT: This article presents an overview of the generalized negative-refractive-index transmission-line (G-NRI-TL) and summarizes the design equations that determine the frequencies of each of its four passbands. Specific multiband devices to which G-NRI-TLs have been applied are discussed: both a dual-band coupled-line coupler operating at 2.7 and 4.7 GHz and a printed single-ended all-pass cell with two pairs of right- and left-handed bands are explained. The details of how each may be fabricated in a fully-printed layout are provided and simulated and measured results are given. © 2012 Wiley Periodicals, Inc. Int J RF and Microwave CAE 22:459–468, 2012.

Keywords: all-pass network; artificial transmission line; coupler; generalized negative-refractive-index transmission-line; impedance inverter; metamaterial

I. INTRODUCTION

Formed by loading a conventional transmission line with a series capacitor and a shunt inductor, negative-refractive-index transmission lines (NRI-TLs) have found a wide variety of uses in microwave components. Multiband versions of these components are possible using the Generalized NRI-TL (G-NRI-TL), another type of artificial transmission line which forms a one-dimensional (1D) metamaterial. First reported in Ref. [1], the G-NRI-TL has since been applied to leaky-wave antennas, filters, power dividers, and couplers [2–4]; its important feature is two pairs of right-handed (forward) and left-handed (backward) propagating bands separated by a stopband. These four bands give the unit cell a single electrical length at four different frequencies, thus enabling multiband performance. As was shown in Ref. [1], if the circuit components comprising the G-NRI-TL cell satisfy certain conditions, the stopbands that exist between the alternating right- and left-handed bands can be closed just as in the conventional NRI-TL case. Moreover, in a more recent development in Refs. [5, 6] the stopband separating the two pairs of bands themselves can be closed, thus allowing for all-pass behavior, while still permitting a positive or negative transmission phase shift to be specified. In all cases, the fabrication of these devices is straightforward, as the underlying topology is that of a microstrip line loaded with the requisite printed components. In this article, we review the theory of both the G-NRI-TL and its all-pass version and also present some of the devices to which they have been applied.

This article is organized as follows. Section II gives an overview of the generalized NRI-TL cell and derives the required design equations. Section III presents a multiband coupled-line coupler based on the G-NRI-TL. The all-pass cell is presented in Section IV, along with a discussion of its promising applications. Conclusions and some final remarks are made in Section V.

II. GENERALIZED NRI-TL UNIT CELL

Equivalent Circuit and Dispersion Properties

The topology of the G-NRI-TL and its typical dispersion diagram are shown in Figures 1a and 1b, respectively. The unit cell consists of four pairs of *L-C* resonators, each tuned to the same resonant angular frequency of ω_0. There are now two pairs of right- and left-handed bands in the dispersion diagram separated by a stopband centered at ω_0. Applying standard periodic analysis to the unit cell yields the following dispersion Eq. (1):

$$\cos(\beta d) = 1 + Z_B Y_B \tag{1}$$

Correspondence to: G. V. Eleftheriades; e-mail: gelefth@waves.utoronto.ca

DOI 10.1002/mmce.20636

Published online 25 April 2012 in Wiley Online Library (wileyonlinelibrary.com).

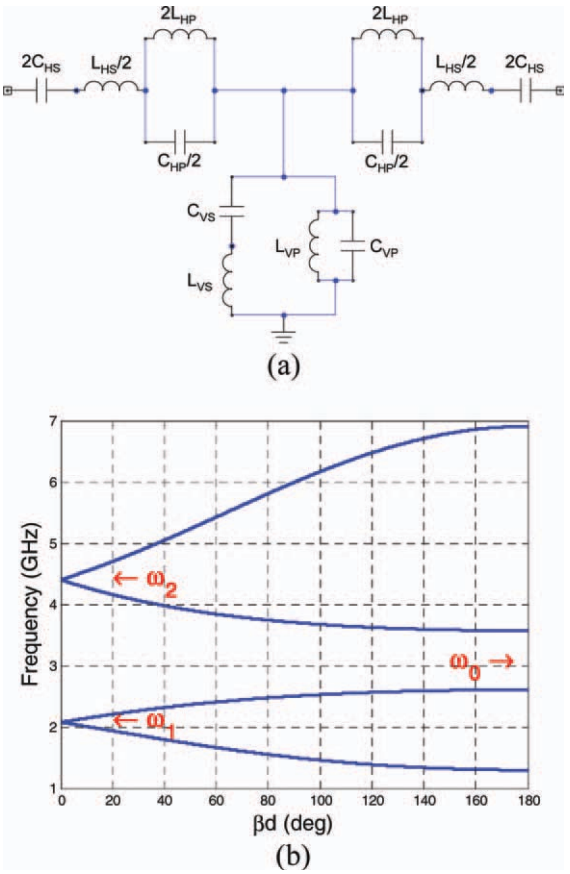

Figure 1 (a) Circuit diagram of G-NRI-TL unit cell and (b) Sample dispersion diagram of G-NRI-TL cell with closed stopbands at ω_1 and ω_2. [Color figure can be viewed in the online issue, which is available at wileyonlinelibrary.com.]

where

$$Z_B = \frac{j\omega L_{HS}}{2} + \frac{1}{j\omega 2C_{HS}} + \left(\frac{j\omega C_{HP}}{2} + \frac{1}{j\omega 2L_{HP}}\right)^{-1}$$
$$Y_B = j\omega C_{VP} + \frac{1}{j\omega L_{VP}} + \left(j\omega L_{VS} + \frac{1}{j\omega C_{VS}}\right)^{-1}$$

The stopbands at ω_1 and ω_2 may be closed under the condition

$$L_{HS}C_{HP} = 4L_{VS}C_{VP} \tag{2}$$

Equation (2) results in the series and shunt branches being short- and open-circuited simultaneously, leading to propagation with a zero transmission phase (i.e., the $\beta d = 0$ frequencies).

Bloch Impedance

In the limit $\beta d \ll 1$, the Bloch impedance of the unit cell is given by

$$Z_{Bloch} = \sqrt{\frac{2Z_B}{Y_B}} \tag{3}$$

which, under the closed stopband condition of (2) simplifies to

$$Z_{Bloch} = \sqrt{\frac{L_{HS}}{C_{VP}}} \tag{4}$$

Therefore, with the appropriate choices for the circuit element values, the G-NRI-TL can be matched to any arbitrary system impedance.

Design Principles

In Ref. [6], it was shown how a single phase shift per unit cell ($\beta d = \varphi$) could be specified at four different angular frequencies ω_1, ω_2, ω_3, and ω_4. The entire derivation is not repeated here, but the final design equations are given below.

The element values are given by

$$\begin{aligned} C_{VP} &= \frac{A}{C_1} & L_{HS} &= q^2 C_{VP} \\ L_{VP} &= \frac{1}{\omega_{VP}{}^2 C_{VP}} & C_{HS} &= \frac{1}{\omega_{VP}{}^2 L_{HS}} \\ L_{VS} &= \frac{1}{\omega_{VPVS}{}^2 C_{VP}} & C_{HP} &= \frac{4L_{VS}C_{VP}}{L_{HS}} \\ C_{VS} &= \frac{1}{\omega_{or}{}^2 L_{VP}} & L_{HP} &= \frac{1}{\omega_{or}{}^2 C_{HP}} \end{aligned} \tag{5}$$

where

$$\begin{aligned} Z_{Bloch} &= \sqrt{\frac{2Z_B}{Y_B}} = q \\ A^2 &= \frac{1-\cos(\phi)}{2q^2} \\ \omega_{or}{}^2 &= \frac{C_3}{C_1} \\ \omega_{VP}{}^2 &= \frac{C_0 C_1}{C_3} \\ \omega_{VPVS}{}^2 &= \left(C_2 - \frac{C_0 C_3}{C_1} - \frac{C_1}{C_3}\right) \\ C_{VP} &= \frac{A}{C_1} \end{aligned} \tag{6}$$

and

$$\begin{aligned} C_0 &= \omega_1\omega_2\omega_3\omega_4 \\ C_1 &= \omega_4 - \omega_3 + \omega_2 - \omega_1 \\ C_2 &= \omega_1\omega_2 - \omega_1\omega_3 + \omega_1\omega_4 + \omega_2\omega_3 - \omega_2\omega_4 + \omega_3\omega_4 \\ C_3 &= -\omega_1\omega_2\omega_3 + \omega_1\omega_2\omega_4 - \omega_1\omega_3\omega_4 + \omega_2\omega_3\omega_4 \end{aligned} \tag{7}$$

The details of how the G-NRI-TL is constructed in microstrip technology and how the required circuit values are synthesized by printed components will be discussed for each of the particular applications in the following sections.

Dual-Band Coupled-Line Coupler

A single-band coupled line coupler comprising a microstrip (MS) transmission line and a G-NRI-TL was first reported in Ref. [4], and in further analysis in Ref. [7], it was shown that such backward coupling occurs at the frequency where the dispersion curves of the isolated

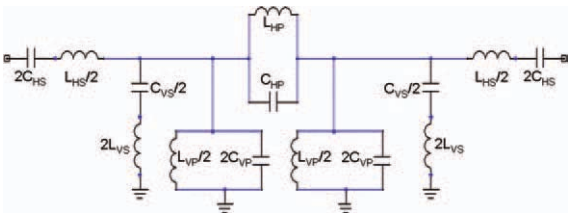

Figure 2 Equivalent circuit for a modified G-NRI-TL unit cell. [Color figure can be viewed in the online issue, which is available at wileyonlinelibrary.com.]

microstrip line and of the left-handed propagation band of the NRI transmission line intersect. An interesting property (variously reported in Ref. [7–9]) was the higher coupling level possible in the MS/NRI-TL coupler compared with traditional microstrip edge couplers of similar dimensions. In Ref. [10], it was observed that one of the modes in the stopband exhibits negative group velocity despite the coupler being formed from an ideally lossless circuit; the observed negative-group-delay allows the coupler to offer inherent phase equalization attributes.

In this section, we show how the two left-handed bands of the G-NRI-TL are exploited to create a dual-band and fully-printed MS/G-NRI-TL edge coupler [11]. Previously, dual-band couplers were based on quadrature or rat-race topologies (e.g., [12–14]) and usually relied on NRI-TLs to synthesize 90° line lengths at two different frequencies. As in Ref. [3], this concept could be expanded to include generalized NRI-TLs, thereby yielding four operating bands; however, this approach may lead to a larger board area than that required by a coupled-line coupler. An additional disadvantage of the quadrature topology is its potentially higher loss: a multi-band quadrature coupler requires at least four G-NRI-TL cells, whereas the edge coupler designed here uses three. It is desirable to limit the number of G-NRI-TL cells, as they typically comprise many fine features that increase the overall conductor losses. As will be seen, good performance is obtained from this new design, as it either meets or exceeds previously reported results.

Equivalent Circuit Design

The circuit diagram of the unit cell used in the G-NRI-TL section of the coupler is shown in Figure 2. Derived from the π-model of a single-band NRI-TL equivalent circuit, it is a modification of the T-model cell presented in the preceding section but still possesses two pairs of right- and left-handed propagation bands. The advantage of this layout lies in its single C_{HP}/L_{HP} resonator, which reduces fabrication complexity of its printed counterpart. Furthermore, a true π-model circuit would have the C_{HS}/L_{HS} resonators immediately on either side of the central element. Here, they are moved to the cell terminations, as the length of transmission line required to synthesize both the C_{HP} and C_{HS} capacitances means they have to be spaced relatively far apart; to reduce the overall cell length, the shunt elements are incorporated into this space. The desired circuit values for the coupler are given in Table I.

Printed Unit Cell

An illustration of the fully printed cell is given in Figure 3 with the corresponding circuit elements and dimensions labeled. It should be noted that L_{HS} and C_{VP} are distributed elements forming the transmission line. The capacitances C_{HS} and C_{HP} are synthesized by parallel plates which yield a constant capacitance over a larger bandwidth than would an interdigitated capacitor. As shown in the figure, these parallel plates overlap on one side of the trace only; on the other side, they are directly connected to the main line by vias through the substrate. Therefore, this unit cell comprises three metallization layers (including the ground) and two substrate layers; the L_{VP} vias run from the top-most layer to the ground. Each printed circuit component was simulated individually in HFSS and its geometric parameters were varied to match the frequency response to that of the corresponding circuit; the components were then assembled to form the complete unit cell. The final dimensions of the printed cell are given in Table I.

Multiconductor Transmission Line Analysis

A single unit cell of this coupled-line coupler may be analyzed using multiconductor transmission line (MTL) analysis [15]. Figure 4 shows the equivalent circuit for the device where there are two lines representing the right-handed microstrip line and generalized NRI-TL cell, respectively. The coupling mechanism is accounted for by mutual inductances L_m on both signal lines and by a mutual capacitance C_m between the lines [16].

The propagation properties for the overall cell can be determined from its ABCD matrix. For the 4-port network illustrated in Figure 4, this ABCD matrix takes the form

$$\begin{bmatrix} V_{11} \\ V_{21} \\ I_{11} \\ I_{21} \end{bmatrix} = T_{\text{UnitCell}} \begin{bmatrix} V_{12} \\ V_{22} \\ I_{12} \\ I_{22} \end{bmatrix} \tag{8}$$

where T_{UnitCell} is found by cascading ABCD matrices of each of the individual elements; these expressions are not given here, but may be found in Ref. [11].

TABLE I Summary of Circuit Parameters and Printed Cell Dimensions

Circuit Values		Printed Cell Dimensions	
C_{HS}	0.682 pF	C_{HS} Overlap	0.8 mm
L_{HS}	3.64 nH	C_{HP} Overlap	0.4 mm
C_{HP}	0.928 pF	L_{HP} Gap	1.4 mm
L_{HP}	2.23 nH	L_{HP} Trace Width	0.2 mm
C_{VS}	0.45 pF	C_{VS} Width/Length	3 mm/3.5 mm
L_{VS}	4.64 nH	L_{VP} Length	2.3 mm
C_{VP}	0.72 pF	L_{VP} Width	0.3 mm
L_{VP}	2.27 nH	L_{VS} Length	4.8 mm
		L_{VS} Width	0.3 mm
		Trace Width	5.2 mm
		Layer 1 Height	1.524 mm
		Layer 2 Height	0.127 mm
		Substrate ε_r	2.2
		Microstrip line width	4.8 mm
		MS/G-NRI-TL Separation	0.4 mm

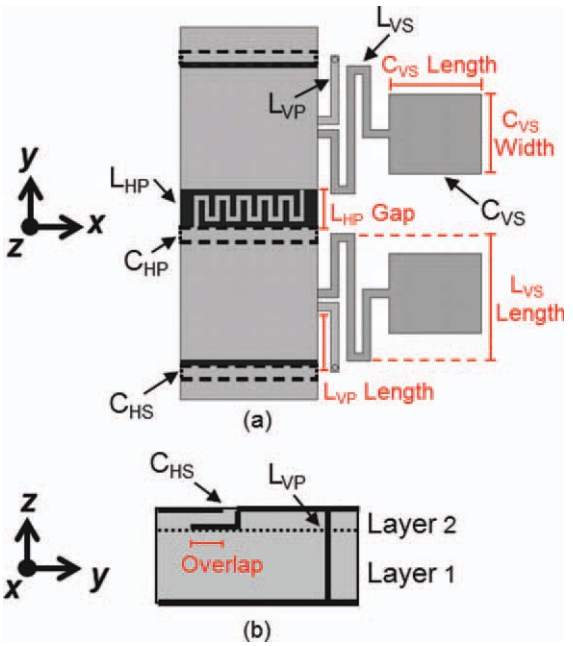

Figure 3 Implementation of a generalized NRI-TL circuit as a fully-printed unit cell for an edge coupler. (a) Top view where dotted lines show areas of overlap for the parallel-plate capacitors and solid black areas denote underlying parallel plates. (b) Side profile view showing C_{HS} and L_{VP} elements with dimensions exaggerated. [Color figure can be viewed in the online issue, which is available at wileyonlinelibrary.com.]

From Figure 4, the overall cell ABCD matrix is

$$T_{Cell} = T_{Series}T_Y T_{CR}T_{HP}T_{LM}T_{CM}T_{CM}T_{LM}T_{HP}T_{CR}T_Y T_{Series}$$

$$T_{Cell} = \begin{bmatrix} A_F & B_F \\ C_F & D_F \end{bmatrix} \tag{9}$$

As described in Ref. [17], the dispersion equation for this lossless, reciprocal, and symmetric unit cell is found from

$$\det(A_F - \cosh(\gamma d)I) = 0 \tag{10}$$

where γ is the propagation constant through the unit cell of length d. The resulting expression for the propagation constant takes the form

$$\gamma d = \alpha \pm j\beta \tag{11}$$

where the plus sign is associated with the so-called γ_C mode which carries power forward on the microstrip line and backward on the G-NRI-TL; the reverse holds true for the minus sign and the γ_π mode.

Using Eq. (10), the dispersion diagram for the coupler was plotted and is shown in Figure 5. The circuit elements of the microstrip line, $L_R = 2.72$ nH and $C_R = 1.1$ pF, were chosen to fit both the dispersion curve and characteristic impedance of the line found from full-wave simulations. In Figure 5a, there is no coupling between the MS and G-NRI-TL lines to identify more easily the dispersion curves of the isolated components; in Figure 5b, coupling is accounted for and the dispersion results calculated from Ansoft HFSS' Eigenmode solver [18] are superimposed on the figure. The circuit component values are as specified in Table I, whereas the mutual inductance and capacitance values were determined to fit the curves, yielding values of $L_m = 1.5$ nH and $C_m = 0.15$ pF. It is seen that good agreement between the two methods is obtained. The graph shows the expected band splitting where the microstrip mode dispersion curve intersects the left-handed bands of the G-NRI-TL cell, and therefore, backward-wave coupling is anticipated at $\sim$ 2.5 and 4.4 GHz.

Simulated Coupler Performance

HFSS was used to analyze the three-cell coupler. As a large number of parametric sweeps were conducted during the optimization process, perfect conductors were assumed to reduce the computational load. However, substrate dielectric losses ($\tan\delta = 0.0009$) were included in the simulation. All ports were terminated with 50 Ω loads. Figures 6 and 7 show the simulated S-parameters as well as the insertion loss (IL) calculated from

$$IL = -10\log\left(|S_{11}|^2 + |S_{21}|^2 + |S_{31}|^2 + |S_{41}|^2\right) \tag{12}$$

The coupling frequencies are well predicted by the analytical and eigenmode solution methods. The peak coupling magnitude at the lower and upper bands is −3.5 and −2.2 dB, respectively, whereas the return loss (S_{11}) and isolation (S_{41}) reach $\sim$ 20 dB. The insertion loss is less

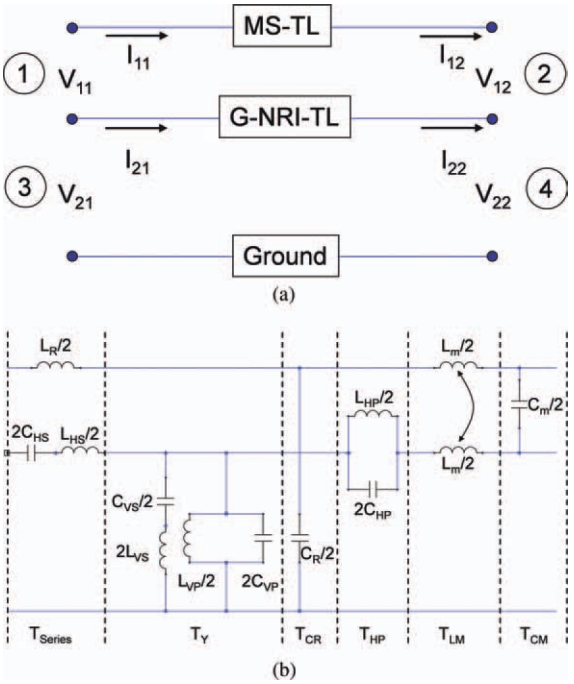

Figure 4 (a) MTL schematic with ports and voltage and current conventions labeled. (b) Equivalent circuit for MTL coupler unit cell. For clarity, only half the unit cell is shown; it is symmetric about the right-most vertical axis. [Color figure can be viewed in the online issue, which is available at wileyonlinelibrary.com.]

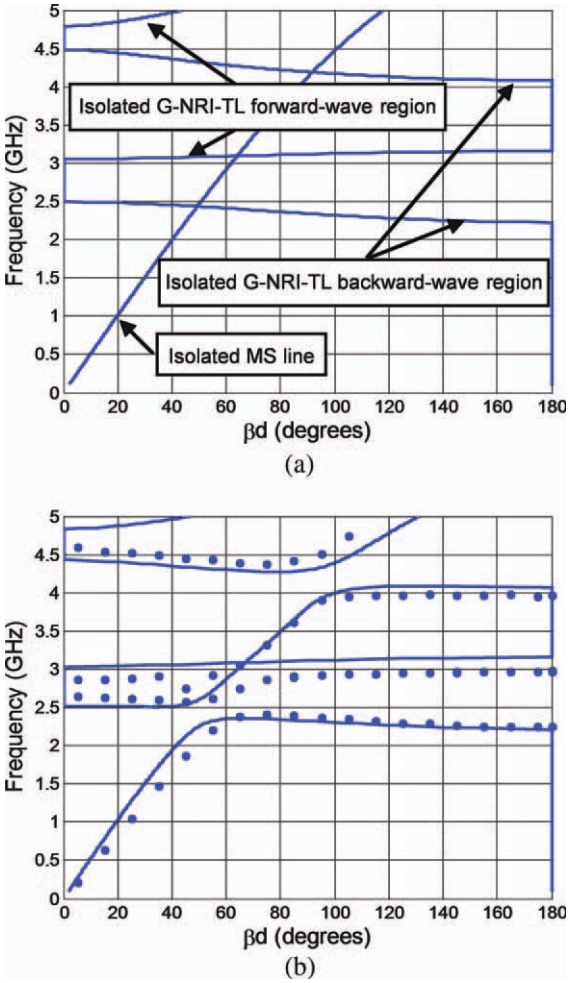

Figure 5 Dispersion diagrams for (a) isolated microstrip TL and G-NRI-TL and (b) dispersion diagram for coupled MS/G-NRI-TL showing analytical solution (solid line) and HFSS full-wave simulation (dots). [Color figure can be viewed in the online issue, which is available at wileyonlinelibrary.com.]

than 0.2 dB over the lower coupling band and less than 0.5 dB over the upper band.

Measured Results

The fabricated coupler is shown in Figure 8. It is manufactured on a Rogers RT/Duroid 5880 substrate ($\varepsilon_r = 2.2$, $\tan\delta = 0.0009$) with a 0.127 mm top layer and a 1.524 mm bottom layer. Measured results are given in Figures 9 and 10 and the coupler shows good agreement with the theoretical performance simulated in HFSS. Peak coupling levels of −3.5 and −4.4 dB are observed at 2.7 and 4.7 GHz, respectively. The return loss is better than 20 dB and the isolation over the two coupling bands is also better than 20 dB; both these parameters either meet or exceed those obtained in Refs. [16, 3], and a significant improvement in the isolation is obtained over that reported in Ref. [19]. The directivity of this coupler is found to be ∼ 20 and 17 dB at the lower and upper bands and is very similar to the results of Ref. [13].

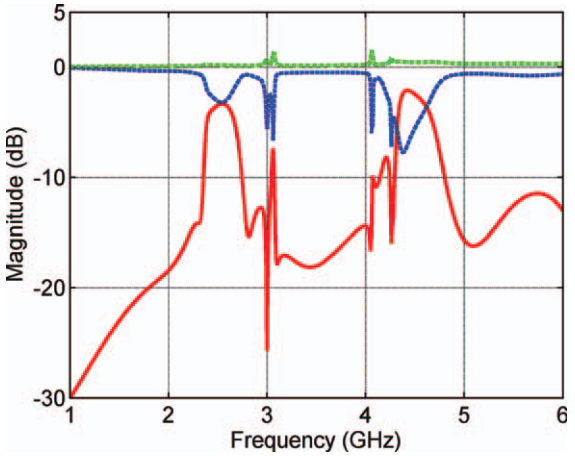

Figure 6 Simulated *S*-parameters for 3-cell edge coupler showing magnitude for coupled (▬), through (▪▪▪), and calculated insertion loss (▪ ▫ ▪). [Color figure can be viewed in the online issue, which is available at wileyonlinelibrary.com.]

The insertion loss calculated from measurements for this coupler over the lower band (a ±2 dB amplitude balance bandwidth of 2.6–2.8 GHz) is usually below 1 dB although reaches 1.4 dB at the band edge; over the upper band from 4.65 to 4.8 GHz, the maximum loss is 1.9 dB but is also typically around 1 dB. These results compare favorably with previous coupler designs: in Ref. [12], a dual-band NRI-TL rat-race coupler had similar losses of 0.9 dB, whereas in Ref. [3], a multiband hybrid coupler based on another version of generalized NRI-TLs suffered insertion losses ranging from 1.6 to 4.7 dB; finally, a dual-band branch-line coupler using only right-handed transmission lines had a maximum insertion losses of 1.3 dB in Ref. [13].

The upward shift in coupling band frequencies can be attributed to errors introduced during the complex fabrication process. The drop in coupling magnitude of 2.2 dB at the upper band may be a result of air gaps between the top

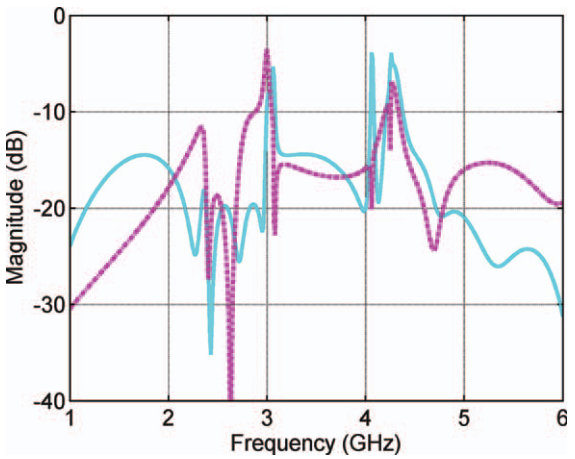

Figure 7 Simulated *S*-parameters for 3-cell edge coupler showing magnitude for reflection (▬) and isolation (▪ ▫ ▪). [Color figure can be viewed in the online issue, which is available at wileyonlinelibrary.com.]

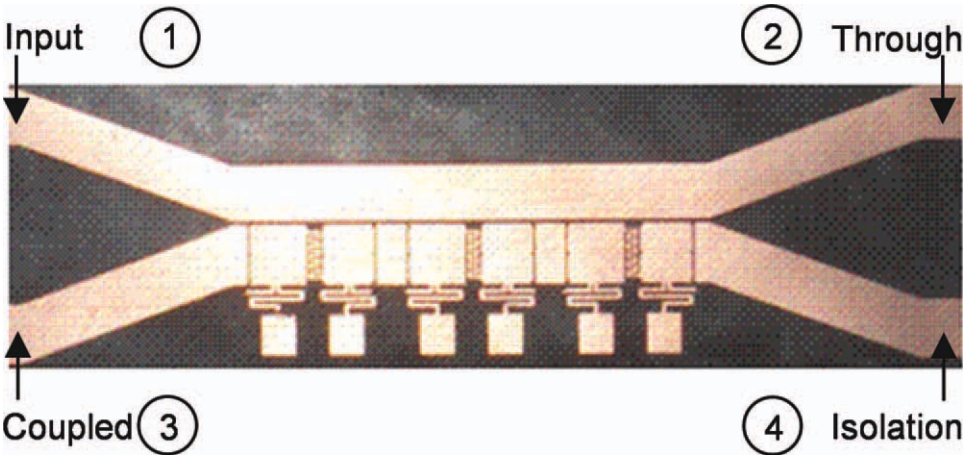

Figure 8 Photograph of fabricated edge coupler with port conventions labeled. The NRI-TL line is 5.2 mm wide, the microstrip line is 4.8 mm wide and the line spacing is 0.4 mm. Including the feed lines, the overall dimensions are width = 30 mm, length = 90 mm. [Color figure can be viewed in the online issue, which is available at wileyonlinelibrary.com.]

and bottom layers which could not be completely eliminated and were not accounted for in the simulation. Furthermore, the length of the shorted stubs was slightly increased as the vias were soldered in place, thus contributing small errors to the final fabricated version; similar difficulties afflicted the connecting vias that were part of the C_{HS} and C_{HP} elements. A comparison of the measured and simulated results is given in Table II. Given both the fabrication complexity and the limits of printed components operating over two widely spaced frequency bands, the correspondence between theoretical and measured results is good.

III. All-Pass G-NRI-TL

The quad-band G-NRI-TL cell discussed previously [and shown again in Figure 11a for reference] has been seen to have a stopband at ω_0 separating the two pairs of right- and left-handed bands. Converting this single-ended circuit to a differential lattice topology [6] eliminates this stopband and creates an all-pass response with low group delay, while preserving the multiband phase characteristics. The drawback of such an approach is that it is difficult to implement as a printed structure due to the small dimensions of the underlying differential transmission line. Moreover, for most applications a single-ended, rather than differential, topology is preferred. Although a lattice arrangement of the standard NRI-TL using CPS lines was reported in Ref. [20], extending this to the generalized version would be difficult for the reasons outlined above. We solve these fabrication

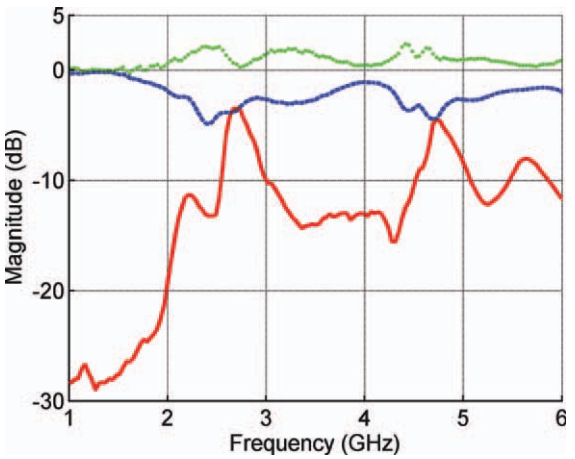

Figure 9 Measured *S*-parameters for 3-cell edge coupler showing magnitude for coupled (), through (), and calculated insertion loss (). [Color figure can be viewed in the online issue, which is available at wileyonlinelibrary.com.]

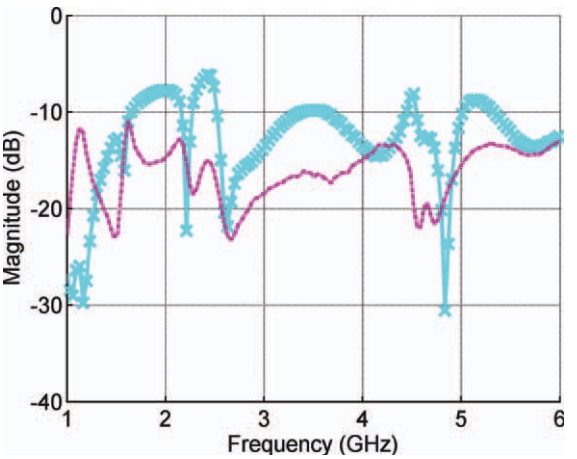

Figure 10 Measured *S*-parameters for three-cell edge coupler showing magnitude for reflection () and isolation (). [Color figure can be viewed in the online issue, which is available at wileyonlinelibrary.com.]

TABLE II Summary of Measured and Simulated Results

Parameter	Simulated	Measured
Coupling Bands (GHz)	2.4–2.7/4.4–4.7	2.6–2.8/4.65–4.8
Maximum Coupling (dB)	−3.5/−2.2	−3.5/−4.4
Maximum Return Loss (dB)	25.17/19.6	21.9/30.6
Maximum Isolation (dB)	27.9/24.3	23.2/21.6
Maximum Directivity (dB)	22.9/19.1	19.7/17.1
Typical Insertion Loss (dB)	0.2/0.5	1.0/1.0

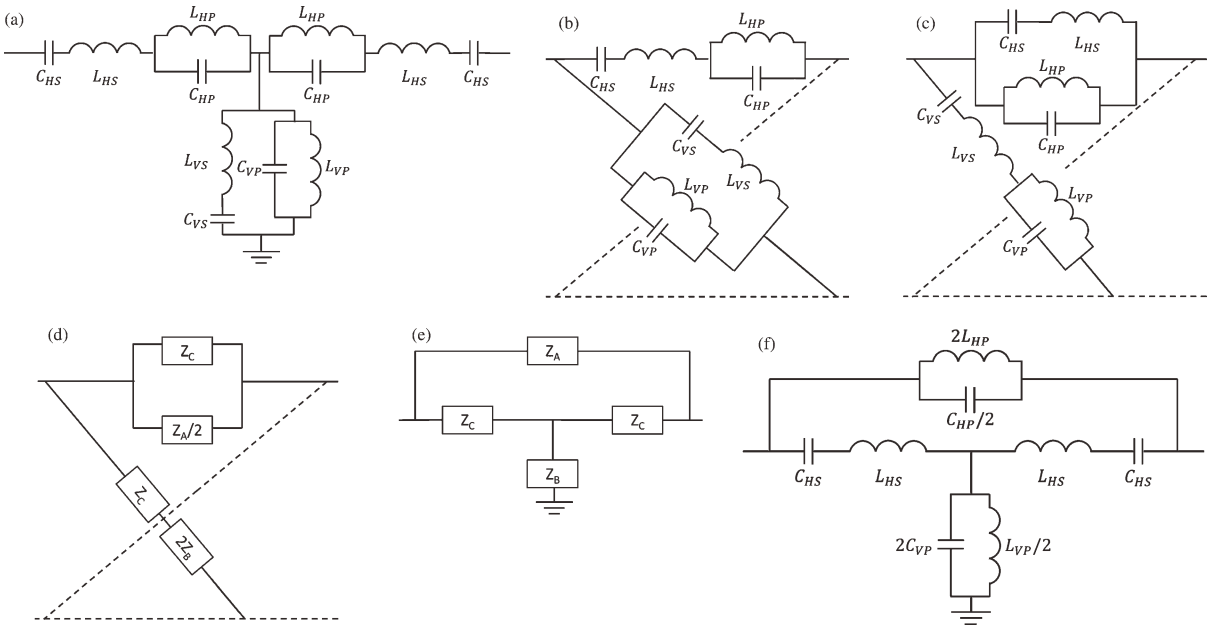

Figure 11 Steps and intermediate circuits necessary for the transformation of a quad-band single-ended cell into an all-pass bridged-T circuit: (a) original quad-band cell; (b) all-pass quad-band lattice; (c) dual version of lattice necessary for transform; (d) and (e) required transform between lattice and bridged-T circuit; (f) final all-pass quad-band bridged-T network. The dashed lines in the lattice networks indicate series and shunt impedances identical to those shown explicitly in the respective circuits.

difficulties using a bridged-T circuit to create a microstrip all-pass single-ended G-NRI-TL.

Lattice to Bridged-T Transformation

As was demonstrated in Ref. [6], if the stopbands of the original cell were closed (i.e., those at ω_1 and ω_2 of Fig. 1), it could be converted into an all-pass type using the lattice topology of Figure 11b. Figure 11c shows the dual version of this lattice, which is necessary to complete the transform as described below. To make this last all-pass circuit suitable for fabrication using microstrip technology, a transform was applied in which the lattice network (Fig. 11d) becomes the bridged-T circuit of Figure 11e [21]. The final circuit diagram is shown in Figure 11f. Note that this transform requires parallel impedances in the series lattice branch, which only appear in the dual lattice of Figure 11c and not in the lattice layout of Ref. [6]. To create this all-pass single-ended circuit, the element values have to meet two conditions: first, the stopband of the original cell must be closed, and second, the values must be chosen so that the impedances of the lattice's series and shunt branches take the form given in Figure 11d. For the circuit of Figure 11a, the closed-stopband condition is

$$L_{\mathrm{VS}}C_{\mathrm{VP}} = L_{\mathrm{HS}}C_{\mathrm{HP}} \tag{13}$$

The required series and shunt impedance equality is

$$j\omega L_{\mathrm{HS}} + \frac{1}{j\omega C_{\mathrm{HS}}} = j\omega L_{\mathrm{VS}} + \frac{1}{j\omega C_{\mathrm{VS}}} \tag{14}$$

So, assigning $L_{\mathrm{VS}} = L_{\mathrm{HS}}$ and $C_{\mathrm{VS}} = C_{\mathrm{HS}}$ to satisfy (14), the closed-stopband condition then requires $C_{\mathrm{VP}} = C_{\mathrm{HP}}$. For simplicity, all capacitances in the circuit were set to 0.6 pF and all inductances were set to 1.3 nH, thus ensuring all conditions are met. Figure 12a shows the calculated dispersion diagrams for the standard G-NRI-TL, for its lattice equivalent, and for the bridged-T all-pass network; Figure 12b shows the S_{11} and S_{21} parameters for all three circuits, although the magnitude of the S-parameters is identical for the lattice and its bridged-T equivalent, and so those curves overlap. It is observed that while the original G-NRI-TL cell has a transmission zero at 5.8 GHz, the bridged-T circuit displays all-pass behavior. Furthermore, as the dual of the original lattice has been used in its derivation, the progression of the bands is reversed compared with the original T-network (i.e., as frequency increases a forward-wave band is now followed by a backward-wave band). The characteristics of the dual lattice are identical to that of the bridged-T cell and are not shown on the graphs.

Printed All Pass Unit Cell

The bridged-T network was designed in HFSS using a Rogers R3003 substrate ($\varepsilon_r = 3$, $\tan\delta = 0.0013$) and is shown in Figure 13. To make fabrication possible, the bridge section is printed on a thin layer of the same substrate and suspended above the main line by a foam layer. The circuit components L_{HS} and C_{VP} are synthesized by the underlying transmission line. The figure shows the correspondence between the printed components and each of the remaining circuit elements. Each element was simulated in isolation in HFSS to find the dimensions that best matched the desired circuit response; the overall structure's geometry was then optimized around these values.

Figure 14 plots the magnitude and phase of the S-parameters obtained from full-wave simulation in HFSS.

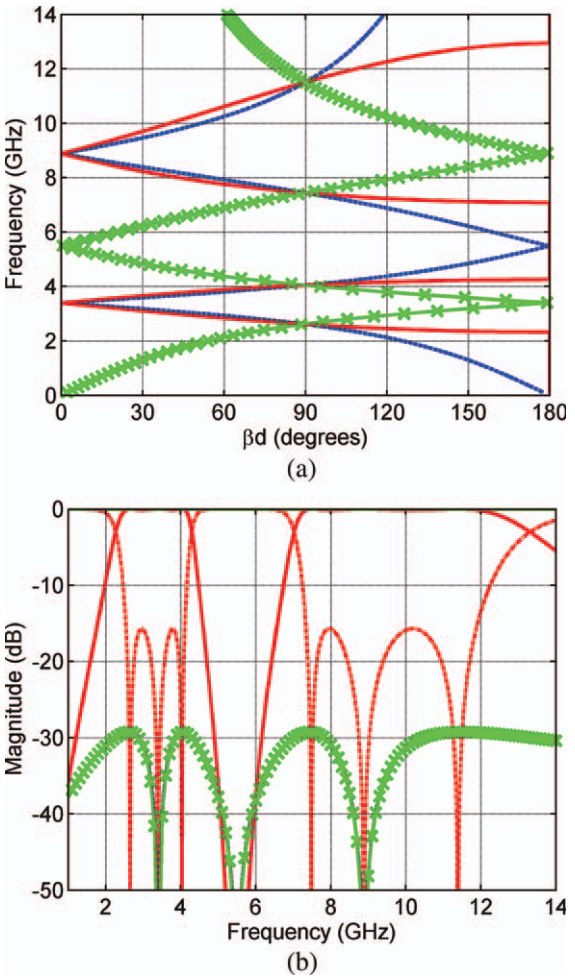

Figure 12 (a)Dispersion curves and (b) *S*-parameter magnitudes for G-NRI-TL T-circuit (▬), its lattice equivalent (▪▪▪), and for Bridged-T circuit (⋆—⋆—⋆). [Color figure can be viewed in the online issue, which is available at wileyonlinelibrary.com.]

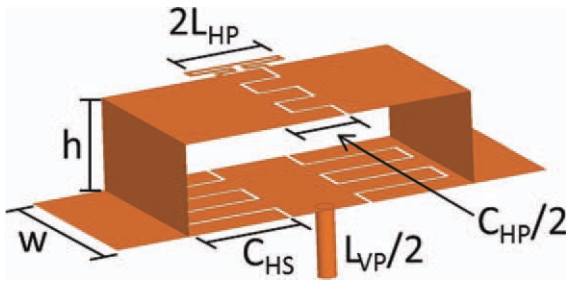

Figure 13 Schematic of printed all-pass cell. For clarity, the substrate layers are not shown and the height of the air gap is exaggerated: $w = 4$ mm, $h = 0.381$ mm, $C_{HS} = 2.25$ mm, $L_{HP} = 2.2$ mm, $C_{HP} = 1$ mm, L_{VP} radius $= 0.4$ mm, finger gap $= 0.1$ mm, cell length $= 14$ mm. The bottom layer has a thickness of 1.524 mm and the top layer of 0.127 mm. [Color figure can be viewed in the online issue, which is available at wileyonlinelibrary.com.]

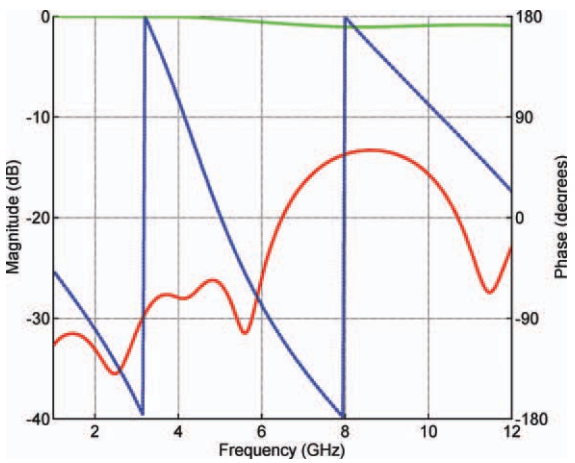

Figure 14 Simulated S_{11} magnitude (▬), S_{21} magnitude (▬) and S_{21} phase (▪▪▪). [Color figure can be viewed in the online issue, which is available at wileyonlinelibrary.com.]

To accommodate an anticipated fabricated version, the cell is longer than that actually required by the circuit-based approach and so the bands are shifted lower in frequency as compared with those in Figure 12. There are two 180° points and one 0° point at approximately the frequencies predicted by the circuit model; note that the response begins to degrade at higher frequencies due to the limited bandwidth of the printed components. Nevertheless, all-pass behavior is achieved over a very wide bandwidth.

Quad-Band Impedance Inverter

One potential application for the all-pass quad-band unit cell is as a quad-band impedance inverter. Here, a 100 Ω load is transformed to a 25 Ω resistance at the input at four different frequencies, corresponding to the points, where the electrical length of the cell is 90°. Figure 15 plots the S_{11} response from full-wave simulation where Port 1 has been renormalized to an impedance of 25 Ω. It is seen that the impedance is indeed matched at the frequencies expected from Figure 14.

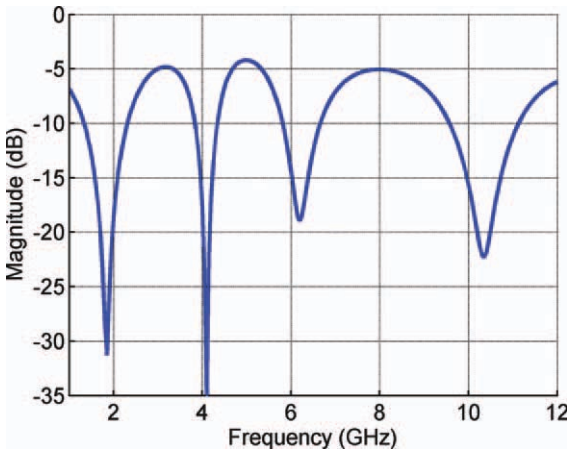

Figure 15 Simulated reflection coefficient (S_{11}) for the quad-band impedance inverter. [Color figure can be viewed in the online issue, which is available at wileyonlinelibrary.com.]

IV. CONCLUSIONS

Generalized negative-refractive-index transmission lines have shown their value in creating multiband microwave components. A dual-band coupler has been fabricated which operates at 2.7 and 4.7 GHz, and an all-pass cell with a simulated pass-band from 1 to 12 GHz has been presented, leading to a quad-band impedance inverter. This single-ended all-pass version of the G-NRI-TL is a particularly interesting development and we are currently exploring several methods of fabrication to exploit its advantages.

Implemented in printed microstrip topology, G-NRI-TLs reduce the cost of a device and simplify its fabrication process as compared with one produced with multiple lumped elements. Although a challenging aspect in their use is the design of printed structures that can operate over large bandwidths, the devices we have created have displayed good agreement with theoretically predicted behavior. The demand for greater data rates in mobile devices, the opening of new frequencies in the RF spectrum, and the ubiquity of potential applications mean that these G-NRI-TLs are well-suited to become indispensable components in microwave transceiver systems.

REFERENCES

1. G.V. Eleftheriades, Design of generalised negative-refractive-index transmission lines for quad-band applications, IET Microwaves, Antennas, and Propagation (Special Issue of Metamaterials) 4 (2010), 977–981.
2. C.G.M. Ryan and G.V. Eleftheriades, A dual-band leaky wave antenna based on generalized negative-refractive-index transmission lines, IEEE International Symposium on Antennas and Propagation, Toronto (Canada), July 11–17, 2010, pp.1–4.
3. M. Duran-Sindreu, G. Siso, J. Bonache, and F. Martin, Planar multi-band microwave components based on the generalized composite right/left handed transmission line concept, IEEE Trans Microwave Theory Tech 58 (2010), 3882–3891.
4. R. Islam and G.V. Eleftheriades, A planar metamaterial co directional coupler that couples power backwards, IEEE MTT-S International Microwave Symposium Digest 1 (2003), 321–324.
5. C.G.M. Ryan and G.V. Eleftheriades, A single-ended all-pass generalized negative-refractive-index transmission line using a bridged-T circuit, to be presented at IEEE International Microwave Symposium, Montreal (Canada), 2012.
6. L. Markley and G.V. Eleftheriades, Quad-band negative-refractive-index transmission-line unit cell with reduced group delay, IET Electron Lett 46 (2010), 1206–1208.
7. R. Islam, F. Elek, and G. V. Eleftheriades, Coupled-line metamaterial coupler having co-directional phase but contra-directional power flow, IEE Electron Lett 50 (2004), 315–317.
8. C. Caloz and T. Itoh, A novel mixed conventional microstrip and composite right/left-hand backward-wave directional coupler with broadband and tight coupling characteristics, IEEE Microwave Wireless Compon Lett 14 (2004), 31–33.
9. E. Jarauta, M.A.G. Laso, T. Lopetegi, F. Falcone, M. Beruete, J.D. Baena, A. Marcotegui, J. Bonache, J. García, R. Marqués, and F. Martín, Novel microstrip backward coupler with metamaterial cells for fully planar fabrication techniques, Microwave Opt Technol Lett 48 (2006), 1205–1209.
10. H. Mirzaei and G.V. Eleftheriades, Negative and zero group velocity in microstrip/negative-refractive-index transmission line couplers, IEEE MTT-S International Microwave Symposium Digest (2010), 37–40.
11. C.G.M. Ryan and G.V. Eleftheriades, Design of a printed dual-band coupled-line coupler with generalised negative-refractive-index transmission lines, IET Microwaves, Antennas & Propagation, in press.
12. I.-H. Lin, M. DeVincentis, C. Caloz, and T. Itoh, Arbitrary dual-band components using composite right/left-handed transmission lines, IEEE Trans Microwave Theory Tech 52 (2004), 1141–1149.
13. L.K. Yeung, A compact dual-band 90° coupler with coupled-line sections, IEEE Trans Microwave Theory Tech 59 (2011), 2227–2232.
14. J. Bonache, G. Sisó, M. Gil, A. Iniesta, J. García-Rincón, and F. Martín, Application of composite right/left handed (CRLH) transmission lines based on complementary split ring resonators (CSRRs) to the design of dual band microwave components, IEEE Microwave Wireless Compon Lett 18 (2008), 524–526.
15. J.A. Brandao Faria, Multiconductor transmission-line structures, Wiley: New York, 1993.
16. C. Caloz, A. Sanada, and T. Itoh, A novel composite right-/left-handed coupled-line directional coupler with arbitrary coupling level and broad bandwidth, IEEE Trans Microwave Theory Tech 52 (2004), 980–992.
17. F. Elek and G.V. Eleftheriades, Dispersion analysis of the shielded Sievenpiper structure using multiconductor transmission-line theory, IEEE Microwave Wireless Compon Lett 14 (2004), 434–436.
18. Available: http://www.ansys.com. Ansoft HFSS v.10, The 3D, electro-magnetic, finite-element simulation tool for high-frequency design, Ansoft Corp., 2005, accessed October 1, 2010.
19. S.-H. Mao and M.-S. Wu, A novel 3-dB directional coupler with broad bandwidth and compact size using composite right/left-handed coplanar waveguides, IEEE Microwave Wireless Compon Lett 17 (2007), 331–333.
20. F. Bongard, J. R. Mosig, A novel composite right/left-handed unit cell and potential antennas applications, IEEE APS International Symposium, San Diego (California), July 5–11, 2008, pp.1–4.
21. H.W. Bode, Network analysis and feedback amplifier design, D. Van Nostrand Company: New York, 1945.

BIOGRAPHIES

Colan G. M. Ryan received the B.A.Sc. degree in Electrical Engineering from the University of Ottawa, in Ottawa, ON, Canada, in 2007 and the M.A.Sc. degree in Electrical Engineering from the Royal Military College of Canada, in Kingston, ON, Canada, in 2009. He is currently working toward his Ph.D. degree in Electrical Engineering at the University of Toronto, Toronto, ON, Canada. His main research interests are antennas, periodic structures, and transmission-line metamaterials.

George V. Eleftheriades earned his Ph.D. and M.S.E.E. degrees in Electrical Engineering from the University of Michigan, Ann Arbor, in 1993 and 1989, respectively, and a diploma in Electrical Engineering from the National Technical University of Athens, Greece in 1988. From 1994 to 1997, he was with the Swiss Federal Institute of Technology in Lausanne. Currently he is a Professor in the Department of Electrical and Computer Engineering at the University of Toronto where he holds the Canada Research Chair/Velma M. Rogers Graham Chair in Engineering. **Prof. Eleftheriades** has served as an IEEE Antennas and Propagation Society (AP-S) Distinguished Lecturer (2004–2009) and as a member of the IEEE APS Administrative Committee (AdCom, 2008–2010). He is an associate editor of the IEEE TRANSACTIONS ON ANTENNAS AND PROPAGATION and a member of Technical Coordination Committee MTT-15 (Microwave Field Theory). He has been the general chair of the 2010 IEEE Intl. Symposium on Antennas and Propagation and CNC/USNC/URSI Radio Science Meeting held in Toronto. He was the recipient of the 2008 IEEE Kiyo Tomiyasu Technical Field Award. He was the recipient of the 2001 Ontario Premiers' Research Excellence Award and the 2001 Gordon Slemon Award presented by the University of Toronto. He was also the recipient of the 2004 E.W.R. Steacie Fellowship presented by the Natural Sciences and Engineering Research Council of Canada. He is the corecipient (with Loic Markley) of the inaugural 2009 IEEE Microwave and Wireless Components Letters Best Paper Award. One of his papers (with Ashwin Iyer) received the RWP King Best Paper Award in 2008. In 2009, Prof. Eleftheriades has been elected a Fellow of the Royal Society of Canada. **Professor Eleftheriades** research interests include transmission-line and other electromagnetic metamaterials, small antennas and components for wireless communications, passive and active microwave components, near-field imaging techniques, plasmonic and nanoscale optical structures, fundamental electromagnetic theory and electromagnetic design of high-speed interconnects.